JAMES | Journal of Advances in Modeling Earth Systems®

RESEARCH ARTICLE
10.1029/2023MS003992

Toward More Accurate Modeling of Canopy Radiative Transfer and Leaf Electron Transport in Land Surface Modeling

Yujie Wang[1] and **Christian Frankenberg**[1,2]

[1]Division of Geological and Planetary Sciences, California Institute of Technology, Pasadena, CA, USA, [2]Jet Propulsion Laboratory, California Institute of Technology, Pasadena, CA, USA

Key Points:

- Hyperspectral canopy radiative transfer model is used to assess the biases in electron transport, photosynthesis, and fluorescence
- Vegetation gross primary productivity and solar-induced fluorescence may be substantially biased in broadband radiative transfer models
- Approaches are provided for broadband radiative transfer models

Supporting Information:

Supporting Information may be found in the online version of this article.

Correspondence to:

Y. Wang,
wyujie@caltech.edu

Citation:

Wang, Y., & Frankenberg, C. (2024). Toward more accurate modeling of canopy radiative transfer and leaf electron transport in land surface modeling. *Journal of Advances in Modeling Earth Systems*, *16*, e2023MS003992. https://doi.org/10.1029/2023MS003992

Received 18 OCT 2023
Accepted 12 MAR 2024

Author Contributions:

Conceptualization: Yujie Wang
Data curation: Yujie Wang
Formal analysis: Yujie Wang, Christian Frankenberg
Funding acquisition: Christian Frankenberg
Investigation: Yujie Wang, Christian Frankenberg
Methodology: Yujie Wang, Christian Frankenberg
Project administration: Christian Frankenberg
Software: Yujie Wang
Supervision: Christian Frankenberg
Validation: Yujie Wang

Abstract Modeling leaf photosynthesis is essential for quantifying the carbon, water, and energy fluxes of the terrestrial biosphere. However, due to the lack of simultaneous measurements of leaf light absorption and gas exchange, canopy radiative transfer (RT) and photosynthesis modeling often rely on simplified assumptions about light absorption and electron transport. These assumptions ignore variations in leaf biophysical traits and environmental conditions. In this study, we utilized a next-generation land surface model (LSM)—CliMA Land, which incorporates hyperspectral canopy RT and provides a more accurate representation of trait variations. We evaluated the potential bias in electron transport estimates introduced by the broadband RT schemes used in traditional LSMs. Additionally, we explored the impact of different leaf electron transport parameterization schemes on global-scale photosynthesis and fluorescence modeling. We showed that (a) traditional LSMs that disregard the impacts of leaf temperature and leaf traits on electron transport tend to overestimate electron transport rates. (b) Photosynthesis and fluorescence within a grid can exhibit biases exceeding 20%, with these biases demonstrating contrasting seasonality. (c) Global estimates of integrated photosynthesis and fluorescence differ by 8.1% and 8.8%, respectively. These results underscore the importance of adopting more sophisticated and accurate modeling schemes, such as hyperspectral canopy RT, in future LSMs and Earth system modeling to enhance the reliability of modeling outcomes.

Plain Language Summary The way sunlight interacts within the forest canopy is often simulated using just two broad channels: one for light that helps plants grow (photosynthetically active radiation) and one for near-infrared light. Unfortunately, these simulations don't take into account key things about leaves, like their color (determined by chlorophyll). These simplifications mean that the models ignore differences in how different leaves respond to light. For instance, green light is more common in the lower canopy, but the models treat it the same as red and blue light. The problem is that plants can use red and blue light more effectively for photosynthesis. So, while these simplified models are faster, they can lead to big mistakes when estimating how much light leaves can absorb and how much they can photosynthesize. To address this issue, we used a more detailed model that considers many different wavelengths of light. We looked at how much the simplified models might mess up estimates of photosynthesis and fluorescence. Our findings show that these errors can be larger than 20% for specific locations. To help make the simplified models more accurate, we've provided data and formulas that consider differences in leaf traits and light conditions throughout the canopy.

1. Introduction

The terrestrial biosphere plays a significant role in mitigating the impact of anthropogenic CO_2 emissions, sequestering approximately 25% of these emissions through photosynthesis (Friedlingstein et al., 2022). Furthermore, it contributes to atmospheric moisture dynamics by returning around 40% of total land precipitation to the atmosphere through transpiration (Schlesinger & Jasechko, 2014). Thus, accurate modeling of leaf gas exchange is imperative for comprehensively predicting global carbon, water, and energy fluxes. This pursuit is essential not only for assessing the land system's capacity to counteract climate change but also for predicting the Earth's future climate trajectory. Achieving this level of accuracy necessitates vegetation models that skillfully represent both plant responses to environmental factors (such as drought stress and CO_2 fertilization) and the environment itself (such as the light environment).

On one hand, there has been a remarkable surge in depicting stomatal responses to the environment over the past few decades. These efforts span from fitting parameter-based empirical models to more intricate process- and

Visualization: Yujie Wang, Christian Frankenberg
Writing – original draft: Yujie Wang
Writing – review & editing: Yujie Wang, Christian Frankenberg

trait-based optimality models (Ball et al., 1987; Leuning, 1995; Medlyn et al., 2011; Sperry et al., 2017; Wang, Anderegg, et al., 2021; Wang et al., 2020; Wolf et al., 2016). Concurrently, the realm of plant hydraulics has undergone extensive exploration (Tyree & Zimmermann, 2002; Venturas et al., 2017), empowering vegetation models to more accurately capture plants' reactions to drought stress and, consequently, the tree mortality caused by drought (Anderegg et al., 2016; McDowell & Allen, 2015; McDowell et al., 2008). These improvements are crucial to improve the modeling of canopy water dynamics, which further impact the canopy light environment. On the other hand, canopy radiative transfer (RT; see Table 1 for the full list of symbols) modeling is also transitioning from traditional broadband approaches to the more complex hyperspectral schemes (Campbell & Norman, 1998; Féret et al., 2017; Jacquemoud & Baret, 1990; Norman, 1982; van der Tol et al., 2009; Yang et al., 2017). This advancement not only elevates the accuracy of the modeling process but also facilitates remote monitoring of vegetation, for example, the models that simulate leaf and canopy optical properties can be used for trait estimation using spaceborne remote sensing data (Croft et al., 2020; Simard et al., 2011; Wei et al., 2019).

Despite the notable advancements and improved predictive precision they offer (Anderegg et al., 2016; Féret et al., 2021; Sabot et al., 2022; Sperry et al., 2019; Wang et al., 2020), the integration of these progressions into land surface models (LSMs) and Earth system models (ESMs) has encountered significant obstacles. Among the foremost hurdles lies the challenge of data accessibility (Wang et al., 2023). Evidently, the acquisition of labor-intensive plant traits remains an enduring obstacle. Further, extra impediments stem from the intricate nature of the model processes, rendering them computationally intensive for LSMs and ESMs. For example, in contrast to the conventional approach of canopy RT modeling, which utilizes two broadband channels of photosynthetically active radiation (PAR) and near-infrared radiation (NIR) (Campbell & Norman, 1998; Norman, 1982), the adoption of the hyperspectral RT scheme can introduce a slowdown of over 100-fold depending on the number of wavelength bins and canopy layering (Wang & Frankenberg, 2022). This extended computational demand ripples through subsequent photosynthesis and stomatal modeling processes. Notably, these more advanced model schemes allow researchers to more accurately represent the biophysical and physiological vegetation processes, and to learn more from the increasing number of data. The central focus of this study is to investigate the impact of canopy RT modeling on leaf photosynthesis and chlorophyll fluorescence.

In addition to its capacity for modeling canopy optical attributes such as reflectance and fluorescence spectra (van der Tol et al., 2009; Wang, Köhler, et al., 2021; Yang et al., 2017), the hyperspectral canopy RT scheme presents several distinct advantages when compared to the conventional broadband RT scheme. Foremost, hyperspectral RT leverages leaf traits, including chlorophyll content and leaf biomass components, to deduce leaf absorption features (Féret et al., 2017, 2021; Jacquemoud & Baret, 1990). This empowers the model with a more accurate and nuanced representation of vegetation characteristics. Second, the partitioning of absorbed PAR within the leaf is no longer constrained by a constant assumption. Instead, hyperspectral RT computes this partitioning based on intrinsic leaf biophysical properties. This departure from the rigid assumption enables a finer-tuned portrayal of electron transport and partitioning between photosystems (Hogewoning et al., 2012; Laisk et al., 2014). Furthermore, hyperspectral RT is equipped to address the variations in the light source spectrum across the canopy (van der Tol et al., 2009). As an illustration, green light is disproportionately abundant in the lower canopy, yet leaves exhibit a diminished capacity to absorb green light compared to red and blue wavelengths. Unlike the conventional broadband RT scheme, which treats green light equivalently to red and blue light, hyperspectral RT is primed to account for this differential absorption. This critical adjustment holds significant implications for the accurate modeling of canopy energy balance, photosynthesis, and transpiration processes.

The leaf's net photosynthetic rate (A_{net}) is typically represented as the minimum value between the rates limited by carboxylation regeneration (A_c) and electron transport (A_j) in photosynthesis models (Collatz et al., 1992; Farquhar et al., 1980; Johnson & Berry, 2021). In the extensively adopted C3 photosynthesis model by Farquhar et al. (1980), the computation of A_j is expressed as:

$$A_j = \frac{J}{4} \cdot \frac{C_i - \Gamma^*}{C_i + 2\Gamma^*} - R_d, \tag{1}$$

$$J = \frac{J_{max} + J_{PSII} - \sqrt{(J_{max} + J_{PSII})^2 - 4\theta J_{max} J_{PSII}}}{2\theta}, \tag{2}$$

Table 1
List of Symbols

Symbol	Description
A_{net}	Net photosynthetic rate
C_i	Internal CO_2 concentration
J	Potential electron transport rate in photosystem II
J_{max}	Maximum electron transport rate in photosystem II at leaf temperature
J_{PSII}	PAR that excites electrons in photosystem II
R_d	Respiration rate
Γ*	CO_2 compensation point with the absence of R_d
θ	Smoothing curvature to compute J
car	Carotenoid content
Chl	Chlorophyll content
LMA	leaf dry mass per area
PAR	Photosynthetically active radiation
APAR	PAR absorbed by leaf
PPAR	PAR absorbed by the antenna system of the photosystems
f_{APAR}	Fraction of APAR in PAR (APAR/PAR)
f_{PPAR}	Fraction of PPAR in APAR (PPAR/APAR)
f_{PSII}	Fraction of PPAR goes to photosystem II
$\Phi_{PSII,max}$	Maximum photosystem II yield
α	Electron quantum yield ($f_{APAR} \cdot f_{PPAR} \cdot f_{PSII} \cdot \Phi_{PSII,max}$)
GPP	Integrated gross photosynthetic rate of the canopy
SIF	Solar-induced chlorophyll fluorescence
RT	Radiative transfer
LSM	Land surface model
ESM	Earth system model

where J is the potential electron transport rate, C_i is the internal CO_2 partial pressure, Γ* is the CO_2 compensation point with the absence of dark respiration (R_d), J_{max} is the maximum electron transport rate at leaf temperature, J_{PSII} is the potential electron transport in photosystem II (PSII) from total absorbed radiation, and θ ($0 < \theta \leq 1$) is a curvature parameter to smooth J_{max} and J_{PSII}.

The magnitude of J_{PSII} is contingent upon not only the incident PAR but also on key leaf biophysical parameters including leaf pigments, carbon concentration, and water content (Féret et al., 2017; Jacquemoud & Baret, 1990). Mathematically, the expression for J_{PSII} is given by:

$$J_{PSII} = PAR \cdot f_{APAR} \cdot f_{PPAR} \cdot f_{PSII} \cdot \Phi_{PSII,max}, \quad (3)$$

where f_{APAR} is the ratio between total absorbed PAR (APAR) and PAR, f_{PPAR} is the ratio between photosystem antenna absorbed PAR (PPAR) and APAR, f_{PSII} is the fraction of PPAR that goes to PSII (typically assumed to be 0.5), and $\Phi_{PSII,max}$ is the maximum PSII yield (often assumed to be constant, e.g., 0.85 as in Quebbeman and Ramirez (2016)). Although both f_{APAR} and f_{PPAR} are influenced by radiation and trait-related factors (Féret et al., 2021; Grassi et al., 2002), they are seldom directly quantified in leaf gas exchange measurements. In practice, they are often assumed to remain constant, primarily due to the absence of leaf hyperspectral absorption feature data within conventional photosynthesis measurements. Typically in vegetation models, f_{APAR} is equivalent to leaf absorptance in the PAR range whereas f_{PPAR} is assumed to be 1 (namely all APAR goes to the photosystems). For example, in studies such as Medlyn et al. (2002) and Sperry et al. (2017), a value of $\alpha = f_{APAR} \cdot f_{PPAR} \cdot f_{PSII} \cdot \Phi_{PSII,max} = 0.3$ was utilized, while Harley et al. (1992) and Walker et al. (2014) employed $\alpha = 0.24$.

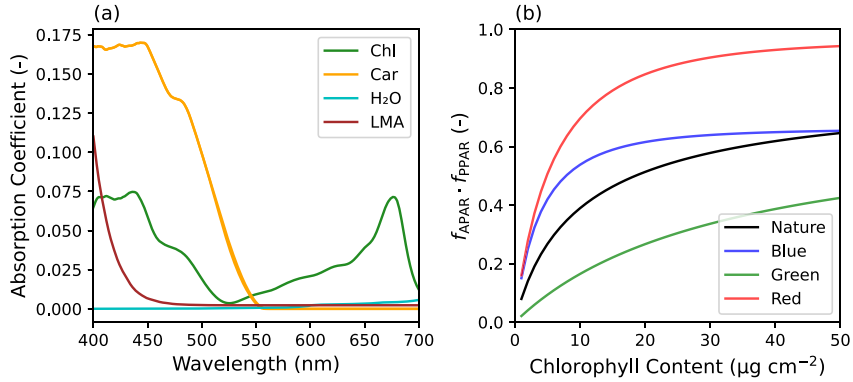

Figure 1. Leaf hyperspectral absorption features and light absorption coefficients. (a) Absorption coefficients of Chl (coefficient unit: $cm^2\ \mu g^{-1}$), car (coefficient unit: $cm^2\ \mu g^{-1}$), water (coefficient unit: cm^{-1}), and LMA (coefficient unit: $cm^2\ mg^{-1}$). (b) The $f_{APAR} \cdot f_{PPAR}$ at different chlorophyll contents and light sources. See Table 1 for the list of symbols. The simulations are done using the PROSPECT leaf radiative transfer model (Féret et al., 2017; Jacquemoud & Baret, 1990) embedded in CliMA Land (Wang et al., 2023; Wang, Köhler, et al., 2021). The $f_{APAR} \cdot f_{PPAR}$ is computed for a leaf with a structure equivalent to 1.4 mesophyll layers (Jacquemoud & Baret, 1990), leaf mass per area of 0.012 g cm^{-2}, and leaf carotenoid content of 1/7 the chlorophyll content (Croft et al., 2020). The natural radiation spectra shapes are from the American Society for Testing and Materials (ASTM) G-173 look-up table, blue light with flat flux density from 448 to 458 nm, green light with flat flux density from 530 to 540 nm, and red light with flat flux density from 655 to 665 nm.

The inability to precisely incorporate the varying factors of f_{APAR},f_{PPAR}, or $\Phi_{PSII,max}$ has the potential to introduce biases into the modeled A_{net}, particularly evident for shaded leaves within the lower canopy that are inherently light-limited. Amongst various contributors, chlorophyll, carotenoid, and leaf biomass prominently contribute to light absorption within the 400–700 nm range (refer to Figure 1a). For instance, as chlorophyll content increases, the product $f_{APAR} \cdot f_{PPAR}$ should also rise and eventually reach a saturation point (depicted in Figure 1b). Notably, different leaf optical models might hold distinct assumptions regarding photosynthetic photon absorption (PPAR), as illustrated by CliMA Land (Wang et al., 2023; Wang, Köhler, et al., 2021). In this case, both chlorophyll and carotenoid absorption are considered a PPAR, recognizing that carotenoid also plays a role within the antenna system. Neglecting the carotenoid's PPAR contribution could lead to an underestimation of $f_{APAR} \cdot f_{PPAR}$. Consequently, being aware of the underlying model assumptions is imperative when utilizing models to compute PPAR.

Due to the non-uniform spectral absorption of leaves in the PAR range, it is crucial to make adjustments to f_{APAR} and f_{PPAR} based on the spectrum of the light source to achieve accurate photosynthesis modeling. Specifically, the highest $f_{APAR} \cdot f_{PPAR}$ values are observed for pure red light (centered around 655–665 nm, as depicted in Figure 1b), whereas pure green light (ranging from 530 to 540 nm, as shown in Figure 1b) leads to the lowest values. Consequently, a cautious approach is necessary when employing empirical correlations between chlorophyll content and f_{APAR} as well as f_{PPAR} (Evans, 1996; Quebbeman & Ramirez, 2016). For instance, the Licor portable photosynthesis system predominantly emits red light peaking at 660 nm (comprising over 90% of the spectrum). In contrast, natural PAR encompasses a more substantial contribution from green light in both direct and diffuse forms. A study by Evans (1996) observed $f_{APAR} \cdot f_{PPAR}$ exceeding 0.9 for leaves possessing high chlorophyll content when subjected to artificial red light (with less than 5% blue light, as indicated by the red curve in Figure 1b). Applying this correlation to leaves exposed to natural light conditions introduces a discrepancy of more than 0.2 in $f_{APAR} \cdot f_{PPAR}$. The magnitude of this difference will increase notably for lower canopy leaves where green light surpasses red and blue light in abundance (as depicted in Figure 1b).

In addition to potential errors introduced by constant assumptions of f_{APAR} and f_{PPAR}, it's important to recognize that the assumption of constant f_{PSII} and $\Phi_{PSII,max}$ can also lead to inaccuracies in computed J_{PSII}. While f_{PSII} is seldom directly measured, it is often approximated as 0.5, reflecting the presumption that plants evenly distribute energy between photosystem I and II for optimal photon absorption under non-stressed conditions. However, it's crucial to note that the partitioning of photons between these photosystems varies with the wavelength of light. Specifically, shorter wavelength photons (below 680 nm) tend to predominantly excite photosystem II, whereas longer wavelength photons tend to overstimulate photosystem I (Hogewoning

et al., 2012; Laisk et al., 2014). Moreover, the light harvest complex on photosystem II can detach and reattach to photosystem I to prevent excessive light from entering photosystem II (Allen et al., 1981). This intricate dynamic justifies the assumption of $f_{APAR} = 0.5$ when shorter wavelength light (below 680 nm) predominates, as it aligns with the avoidance of over-excitation of photosystem II. Nevertheless, when incoming radiation predominantly consists of longer wavelength light (above 680 nm), the $f_{APAR} = 0.5$ assumption and photosynthesis models that disregard photosystem I electron transport could yield problematic outcomes (Porcar-Castell et al., 2021).

When not held as a constant, the computation of $\Phi_{PSII,max}$ typically involves deriving it from the rate coefficients associated with photochemical yield (K_P), fluorescence (K_F), and heat dissipation (K_D). Moreover, recent advancements have incorporated the rate coefficient of sustained non-photochemical quenching (K_S) at lower temperatures into the calculation (Magney et al., 2019; Porcar-Castell, 2011; Raczka et al., 2019):

$$\Phi_{PSII,max} = \frac{K_P}{K_P + K_F + K_D + K_S}. \quad (4)$$

Nonetheless, it's important to recognize that these rate coefficients may exhibit a temperature dependence. For example, van der Tol et al. (2014) advocated the inclusion of temperature dependency within K_D, a step taken to explain the temperature-induced variations in minimum fluorescence after dark adaptation and maximum fluorescence after dark adaptation. Furthermore, Raczka et al. (2019) demonstrated the effectiveness of incorporating a dynamic K_S term at lower temperatures, leading to an enhanced representation of solar-induced chlorophyll fluorescence (SIF) in a sub-alpine forest during winter. Consequently, a more rational approach involves treating $\Phi_{PSII,max}$ as a variable, achieved through the incorporation of temperature-dependent terms within K_D and K_S:

$$K_D = \max(0.0301 \cdot T_{leaf} + 0.0773, 0.8738), \quad (5)$$

$$K_S = \frac{K_{S,max}}{1 + \exp[b \cdot (S - T_s)]}, \quad (6)$$

where T_{leaf} is leaf temperature in °C, [$K_{S,max}$, b, T_s] are fitting parameters, and S is a dynamic acclimation state based on temperature (see Raczka et al. (2019) for more details).

However, traditional LSMs face challenges in accurately incorporating the interplay of leaf traits, light sources, and temperature-dependent electron transport within their radiation and photosynthesis models, as they cannot perform canopy RT at hyperspectral resolution. For instance, the state-of-the-art Community Land Model (CLM; version 5) employs a constant coefficient to convert photosynthetically active radiation (PAR) from energy to photons. Moreover, it adopts a $f_{APAR} \cdot f_{PPAR}$ value ranging from 0.84 to 0.88 based on plant functional types (PFTs; $f_{PPAR} = 1$), rather than leveraging leaf biophysical traits (D. M. Lawrence et al., 2019). The implications of such photosynthesis modeling extend to other vital vegetation processes, including stomatal opening and fluorescence emission. Progress in hyperspectral leaf and canopy RT modeling (Féret et al., 2021; Jacquemoud & Baret, 1990; van der Tol et al., 2009; Yang et al., 2017), coupled with advancements in global plant trait estimation and canopy structure characterization (Croft et al., 2020; Wei et al., 2019), has ushered in the ability to assess the significance of addressing these complexities within LSMs.

In the present study, we ask (a) how $f_{APAR} \cdot f_{PPAR}$ varies vertically in a canopy and spatially across the globe, and how much it may be biased by traditional LSMs, and (b) how global scale photosynthesis modeling is biased by imperfect RT and electron transport modeling. To answer the questions, we conduct the research in the following steps. (a) We compute leaf-level $f_{APAR} \cdot f_{PPAR}$ in a vertically resolved canopy at both site level and global scale utilizing a next-generation LSM—CliMA Land. (b) We conduct global-scale simulations with CliMA Land under four scenarios, incorporating varying settings of $f_{APAR} \cdot f_{PPAR}$ and $\Phi_{PSII,max}$. Subsequently, we compare the modeled gross primary productivity (GPP) and SIF among these scenarios. (c) We explore potential strategies aimed at refining the representation of electron transport within traditional LSMs, thereby seeking to enhance their accuracy in RT and thus photosynthesis modeling.

2. Materials and Methods

2.1. CliMA Land

CliMA Land, available at https://github.com/CliMA/Land, stands as a next-generation, highly modular LSM coded in Julia. Its primary objective is to leverage the growing wealth of remote sensing data beyond carbon and water fluxes (Wang, Köhler, et al., 2021). The remarkable modularity of CliMA Land empowers its deployment in diverse research contexts spanning multiple scales, from leaf to organ, plant, and ecosystem levels. Central to its design philosophy is the separation of the core model from configuration schemes (Wang et al., 2023), thereby affording the flexibility to execute the model under various setups, including emulating other LSMs. CliMA Land operates by encapsulating vegetation processes within fundamental units known as soil-plant-air continua (SPACs) within each grid. Notably, the customization of SPACs allows accommodation of a spectrum of complexities (Braghiere et al., 2023; Wang & Frankenberg, 2022). One of the hallmark features of CliMA Land is its departure from the conventional reliance on PFT-based lookup tables. Instead, each SPAC element incorporates site-specific plant traits, thus better accounting for the spatial and temporal variations of these traits (Wang et al., 2023).

We used CliMA Land v0.1 to perform global simulations in the present study, and the exact version is tagged as "a11," which differs from "a6" used in Wang et al. (2023) in that we (a) used a smoothing factor θ of 0.7 when computing the potential leaf electron transport rate from the maximum electron transport and radiation, (b) fixed a bug in the sunlit leaf APAR calculation, (c) added the option to change SIF excitation wavelength, (d) added an on/off switch to allow $\Phi_{PSII,max}$ to vary with leaf temperature (default is on), (e) extended shortwave radiation wavelength coverage to 300 nm to account for ultraviolet radiation, (f) fixed a bug in updating wind speed's impact leaf boundary layer conductance, (g) added a new feature to prescribe broadband leaf reflectance and transmittance and soil albedo, and (h) added a flexible way to include or exclude carotenoid contribution to PPAR (default is to exclude). Among the various supported model schemes within CliMA Land, we used the following configurations for our global simulations:

- multiple layered canopy with hyperspectral RT (Wang & Frankenberg, 2022; Yang et al., 2017);
- clumping index (CI) implementation (Braghiere et al., 2021);
- hyperspectral soil albedo (Braghiere et al., 2023; Jiang & Fang, 2019);
- leaf level PROSPECT-PRO model that partitioned leaf biomass to carbon-based constituents and proteins (Féret et al., 2021);
- carotenoid absorption defined as PPAR (Wang, Köhler, et al., 2021);
- absorbed far-red light with 700–750 nm wavelength used as APAR (Zhen & Bugbee, 2020);
- empirical stomatal model (Medlyn et al., 2011) along with a tuning factor based on soil moisture (Wang et al., 2023);
- weather drivers prescribed from ERA5 single levels reanalysis data (Hersbach et al., 2020);
- viewing zenith angle at 0°.

We configured CliMA Land using the globally gridded data sets from GriddingMachine, which shares data sets via FTP/HTTP, Julia, Matlab, Octave, Python, and R (Wang et al., 2022). The data sets we used in the present study (labeled as "gm3") included soil color (P. J. Lawrence & Chase, 2007), soil hydraulic parameters (Dai et al., 2019), canopy height (Simard et al., 2011), chlorophyll content (Croft et al., 2020), CI (Wei et al., 2019), leaf area index (LAI) (Yuan et al., 2011), specific leaf area (Butler et al., 2017), photosynthetic capacity (Luo et al., 2021), elevation (Yamazaki et al., 2017), land mask (Hersbach et al., 2020), and PFT map used to derive stomatal parameters (P. J. Lawrence & Chase, 2007). The "gm3" data sets we used in the present study differed from the "gm1" used in Wang et al. (2023) only in the CI map as Wei et al. (2019) data set is more updated and has a better temporal resolution (Li et al., 2023). We refer the readers to https://silicormosia.github.io/blogs/emerald/emerald.html for the benchmarks of CliMA Land global simulations of each version from "a6" to "a11."

2.2. Vertical f_{APAR} and f_{PPAR} Profiles

As red and blue light fractions decrease in the lower canopy (because of upper canopy absorption), it is expected to see the spectrally integrated f_{APAR} and f_{PPAR} varying in a vertically resolved canopy and the profiles should vary with canopy structure and leaf traits. To understand how f_{APAR} and f_{PPAR} vary with canopy structure and leaf traits, we ran CliMA Land at the plant level and performed a sensitivity analysis to three leaf traits and two canopy

structural parameters: chlorophyll content (Chl), carotenoid content (Car), and leaf mass per area (LMA), leaf area index (LAI), and CI (a measure of the canopy's horizontal heterogeneity, lower value means more heterogeneous canopy) (Braghiere et al., 2021).

We first ran the model at our default setting: Chl = 40 μg cm^{-2}, Car = 5.7 μg cm^{-2}, LMA = 0.012 g cm^{-2}, LAI = 3, and CI = 1. Note that because of the limited knowledge of how leaf traits vary vertically in the canopy, we used constant leaf trait profiles in our model. We ran the canopy RT at hyperspectral mode and obtained the incident light spectrum per canopy layer (sum of downward direct light, downward diffuse light, and upward diffuse light). We then computed f_{APAR} and f_{PPAR} per layer based on the leaf traits. For each of the sensitivity tests of Chl, Car, LMA, and LAI, we kept other parameters at their default values and doubled the tested parameter (namely Chl to 80 μg cm^{-2}, Car to 11.4 μg cm^{-2}, LMA = 0.024 g cm^{-2}, and LAI to 6 respectively). For the sensitivity test of CI, we reduced CI to 0.5 while keeping other parameters at their default values.

2.3. Potential Biases in $f_{APAR} \cdot f_{PPAR}$

To further illustrate how leaf absorption features may be biased, we evaluated the impacts from two aspects at the global scale: (a) chlorophyll content and (b) light source. First, we computed annual mean Chl for each 1° × 1° grid from the weekly mean derived based on Medium Resolution Imaging Spectrometer (MERIS) data (Croft et al., 2020). Second, we computed the maximum LAI per grid using the monthly LAI data for the year 2019 (Dai et al., 2019; Wang et al., 2022). Third, we ran the CliMA Land RT module at each grid using the average Chl and maximum LAI, and obtained the incident spectra at the top of the canopy (TOC) and bottom of the canopy (BOC). Last, we used the TOC and BOC radiation spectra to compute the spectrally integrated $f_{APAR} \cdot f_{PPAR}$. The comparison between TOC and BOC per grid would help explain how leaf absorption features differ for leaves at different canopy depths.

Note here that we used average Chl and maximum LAI for illustration purposes. In the global simulations, we used weekly Chl time series per 1° × 1° grid, and computed light spectra of each canopy layer based on the time series of LAI, CI, solar zenith angle, and diffuse light fraction.

2.4. Global Simulations

We performed global simulations using CliMA Land at four contrasting configurations regarding $f_{APAR} \cdot f_{PPAR}$ and K_D. The first scenario was our default where we ran the hyperspectral canopy RT model with spatial + temporal Chl variations and accounted for K_D temperature dependency (we labeled it as HS_KDTD). The second scenario is that we ran the hyperspectral canopy RT model with spatial + temporal Chl variations but used a constant K_D = 0.85 (we labeled it as HS_KDST). The third scenario is that we ran the RT model in broadband mode using the CLM configuration while accounting for K_D temperature dependency (we labeled it as BB_KDTD). When running the model at broadband mode, we still use the same amount of wavelength bins (default is 125 bins from 300 to 2,400 nm), but the spectral shapes per PAR and NIR regions were flat. To run the model at broadband mode, we first computed the leaf level broadband reflectance and transmittance using the PFT fractions per grid. We then used these PFT-based values to replace the computed leaf hyperspectral reflectance and transmittance, for example, all the PAR bins (≤700 nm) have the same PFT-based reflectance and transmittance, and all the NIR bins (>700 nm) have the same PFT-based reflectance and transmittance. We also force f_{PPAR} to be 1 so that computed PPAR equals APAR in the canopy RT module. Mathematically, this is equivalent to using only the PAR and NIR bands. However, to model SIF, we still used leaf pigment contents to derive the SIF matrices (leaf-level fluorescence quantum yield was computed using the broadband model). The last scenario is that we ran the RT model in broadband mode using the CLM configuration and used a constant K_D = 0.85 (we labeled it as BB_KDST).

We ran CliMA Land at 1° × 1° resolution at hourly time step for the year 2019 using the protocol described in Wang et al. (2023). We then re-sampled the simulated results and obtained daily, 8-daily, monthly, and annual means for GPP and SIF at 740 nm. We compared the results among scenarios to determine how the biases in electron transport modeling may impact global photosynthesis modeling. We compared the results using annual and monthly means.

To explore the major drives for the model differences, we used the general linear model to examine how well the combinations of Chl, LMA, LAI, and CI explain the spatial distribution of ΔGPP and ΔSIF (there is no global

scale data set for carotenoid; in our simulations, we assumed Car = Chl/7). For each of the Chl (Croft et al., 2020), LMA (Butler et al., 2017), LAI (Yuan et al., 2011), and CI (Wei et al., 2019) data sets, we resampled the original data set to 1° resolution and took the annual mean. Further, to estimate how the difference in GPP and SIF among scenarios were related to PFT, we used the dominant PFT that has the highest fraction to categorize each grid using the PFT map from P. J. Lawrence and Chase (2007). We selected the following 11 PFTs following the CLM setup (D. M. Lawrence et al., 2019): needle leaf evergreen temperate (NET-P), needle leaf evergreen boreal (NET-B), needle leaf deciduous boreal (NDT-B), broad leaf evergreen tropical (BET-T), broad leaf evergreen temperate (BET-P), broad leaf deciduous tropical (BDT-T), broad leaf deciduous temperate (BDT-P), broad leaf deciduous boreal (BDT-B), evergreen shrub temperate (BES-P), deciduous shrub temperate (BDS-P), and deciduous shrub boreal (BDS-B). We then compared how the GPP and SIF differences between BB_KDST and HS_KDTD scenarios vary with the dominating PFT per grid.

3. Results

3.1. Vertical f_{APAR} and f_{PPAR} Profiles

Because of the changes in the light spectrum in the lower canopy (i.e., lower red and blue light fractions), both spectrally integrated f_{APAR} and f_{PPAR} and thus $f_{APAR} \cdot f_{PPAR}$ decrease in the lower canopy layers (Figure 2). When leaf chlorophyll content increases, the leaf can absorb more photons with the wavelength from 400 to 700 nm (Figure 1a), and a higher fraction of photons goes to the photosystems. Thus, both f_{APAR} and f_{PPAR} increase (Figure 2). When leaf carotenoid content increases, the leaf can only absorb more photons from 400 to 550 nm (Figure 1a) but this extra absorption does not necessarily count into PPAR. As a result, f_{PPAR} and thus $f_{APAR} \cdot f_{PPAR}$ decrease in the lower canopy (Figure 2). Increasing LMA results in higher total light absorption (higher f_{APAR}) but lower photon partitioning to the photosystems (lower f_{PPAR}), and overall $f_{APAR} \cdot f_{PPAR}$ decreases (Figure 2). When LAI increases, blue and red light fractions would further decrease in the lower canopy. Even though leaf-level hyperspectral absorption features are not changing, the spectrally integrated f_{APAR} and f_{PPAR} both decrease (Figure 2). When CI decreases, more light can penetrate through the canopy to the lower layers, and as a result, spectrally weighted f_{APAR} and f_{PPAR} both increase (Figure 2).

3.2. Potential Bias in $f_{APAR} \cdot f_{PPAR}$

The leaf PPAR absorption ratio, denoted as $f_{APAR} \cdot f_{PPAR}$, exhibits significant geographical variation attributed to both spatial and temporal fluctuations in leaf pigments, particularly chlorophyll (refer to Figure 3a for the impact of spatial chlorophyll content variations; LAI has minimum contribution to the TOC values). Beyond chlorophyll content, vertical radiation distribution in the canopy further influences the effective absorption properties of leaves due to chlorophyll's preferential absorption of blue and red light. Consequently, in the lower canopy with higher green light fractions, the effective $f_{APAR} \cdot f_{PPAR}$ ratio is notably lower in contrast to the leaves at the top of the canopy (as illustrated in Figures 3b and 3d). As most traditional LSMs model broadband leaf reflectance and transmittance regardless of leaf biophysical parameters and radiation spectrum, these models could have a biased $f_{APAR} \cdot f_{PPAR}$ (up to >60% relative bias in the boreal regions). The magnitude of this bias is higher for shaded leaves in the lower canopy (as showcased in Figures 3c and 3d for the potential biases of CLM).

3.3. Global GPP and SIF

Compared to the HS_KDTD scenario when both chlorophyll variations and K_D temperature dependency were accounted for, HS_KDST scenario that removed K_d temperature dependency had higher GPP with the highest $\Delta GPP \approx 0.10$ gC m^{-2} day^{-1} in the tropics (Figure 4a). Similarly, HS_KDST SIF overestimated SIF by up to 0.04 mW m^{-2} nm^{-1} sr^{-1} (Figure 4b). Compared to the HS_KDTD scenario, BB_KDTD scenario at broadband mode had higher GPP across the globe with the highest annual mean $\Delta GPP > 1.2$ gC m^{-2} day^{-1} in the tropical regions (Figure 4c). Annually mean SIF, however, showed different spatial patterns from GPP and most regions had lower SIF (Figure 4d). Combining the impacts from BB_KDTD and HS_KDST, scenario BB_KDST also had higher GPP across the globe (Figure 4e), and the overestimation may be >20% in the boreal regions. In comparison, SIF was also lower in most regions except for the arid regions (Figure 4f). When integrated globally, BB_KDST GPP was higher by 8.1% than HS_KDTD, and SIF at 740 nm was lower by 8.8%.

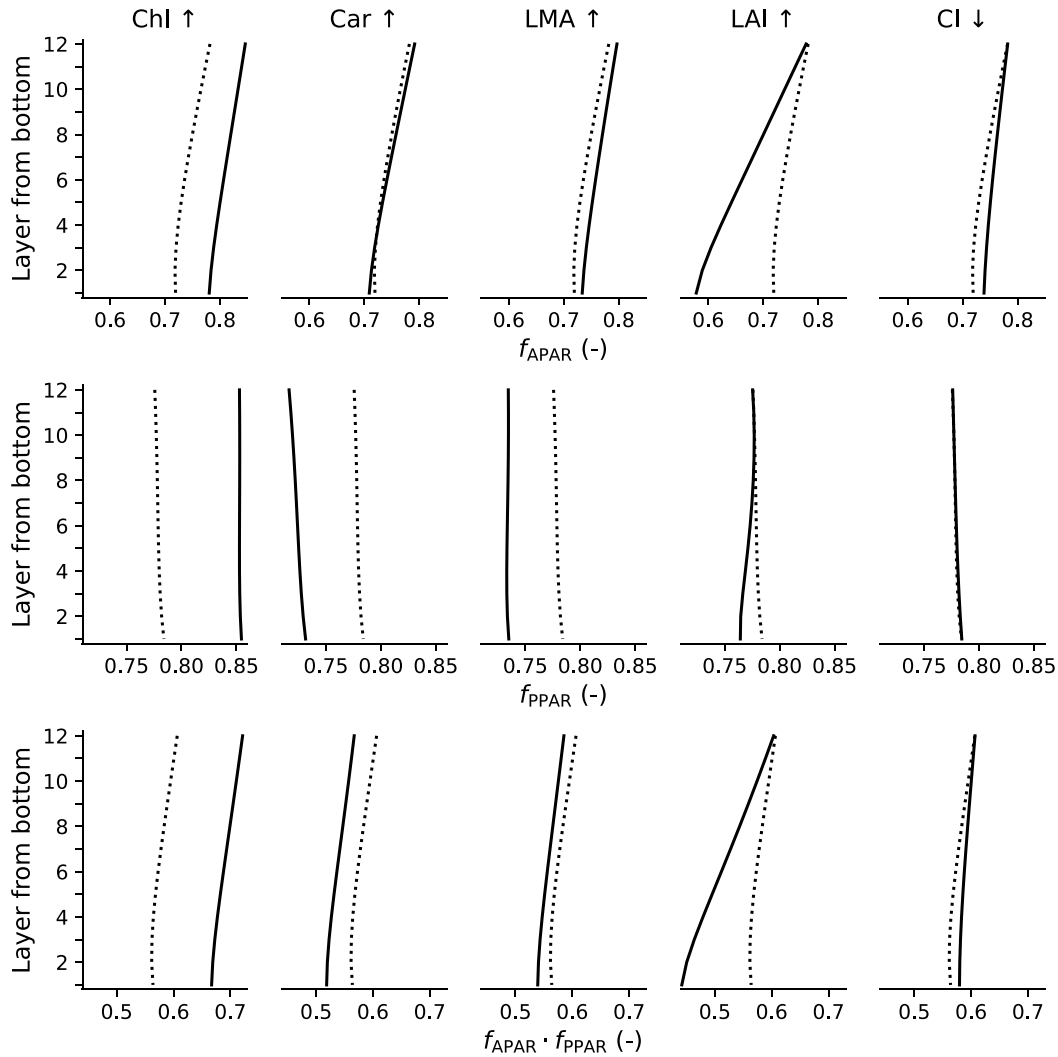

Figure 2. Vertical profiles of f_{APAR} and f_{PPAR} for plants with different leaf traits and canopy structures. Top row: f_{APAR}, middle row: f_{PPAR}, and bottom row: $f_{APAR} \cdot f_{PPAR}$. The dotted curves plot the profiles at the default setting, and the solid curves plot those with higher chlorophyll content (Chl), higher carotenoid content (Car), higher leaf mass per area (LMA), higher leaf area index (LAI) and lower clumping index (CI).

Because of the seasonality of Chl, LAI, and solar radiation, the seasonality of ΔGPP and ΔSIF changed accordingly (see Figure S1 for the comparison between scenarios BB_KDST and HS_KDTD). In general, ΔGPP and ΔSIF showed relatively minor seasonal variations in the tropics, but strong seasonality in the north hemisphere temperate and boreal forests (highest difference in June, July, and August) and in the south hemisphere temperate forests (highest difference in December, January, and February).

The variation of ΔGPP concurred with the LAI spatial pattern ($R^2 = 0.87$ for general linear regression; Table 2). Further adding other parameters into the general linear regression did not improve the R^2 (Table 2). In comparison, LAI explained only 30% of the variation in ΔSIF; however, LAI and Chl together explained 61% of the ΔSIF variation (Table 2). PFT-wise, BB_KDST GPP was always higher than HS_KDTD GPP for all PFTs, and the difference is highest for BET-T, which has the highest LAI (Figure 5a). In comparison, BB_KDST SIF was, in general, higher than HS_KDTD SIF for most of the tested PFTs, except NET-B and NDT-B (Figure 5b). ΔSIF was highest in BET-T and BDT-T, which have the highest annual mean radiation.

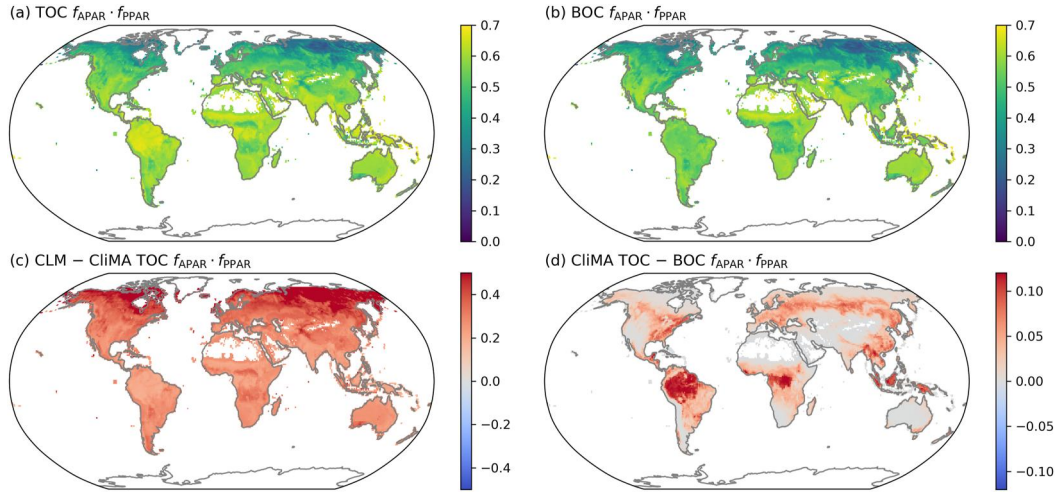

Figure 3. Leaf PPAR absorption ratio and its biases. (a) Top of the canopy (TOC) $f_{APAR} \cdot f_{PPAR}$. (b) Bottom of the canopy (BOC) $f_{APAR} \cdot f_{PPAR}$. (c) Potential bias of TOC $f_{APAR} \cdot f_{PPAR}$ in community land model (CLM) which uses a $f_{APAR} \cdot f_{PPAR}$ around 0.86. (d) Difference between TOC and BOC $f_{APAR} \cdot f_{PPAR}$. Leaf absorption features were simulated using CliMA Land based on the annual mean chlorophyll content from Croft et al. (2020) and maximum LAI of the year 2019 and were meant to illustrate how variations in leaf traits and the light source may impact leaf light absorption features at the global scale. The simulations ignored spatial variations in the other leaf biophysical parameters such as water content and leaf biomass.

4. Discussion

Electron transport within photosynthesis models is often estimated through the application of a constant conversion factor from PAR. Regrettably, this convenient approach tends to overlook the critical influence of leaf biophysical traits and radiation spectra. However, recent strides in modeling hyperspectral RT within canopies and the remote sensing of plant traits have unlocked the potential for a more precise depiction of this process within large-scale LSMs, even though this advancement has incurred substantial computational costs. In this study, we evaluated the potential biases of the traditional LSMs due to their imperfect modeling of canopy RT and electron transport. Leveraging a comprehensive global chlorophyll content map and harnessing the capabilities of a next-generation land model, we conducted a comprehensive assessment. Our findings revealed that the constant conversion factor used in traditional LSMs could yield >60% biases, with the most pronounced discrepancies observed within boreal forests. Additionally, the bias increased within the lower canopy, where the availability of red and blue light is relatively constrained. Building upon these insights, we extended our investigation to assess the impacts of such biased electron transport on global-scale photosynthesis and fluorescence modeling. Our modeled outcomes showed that ignoring variations in leaf biophysical traits and/or the temperature-dependent partitioning of PPAR could lead to biases surpassing 20% in both GPP and SIF. Our results underscore the necessity of incorporating more intricate and realistic biophysical processes within vegetation and land surface models.

We note that the substantial overestimation of GPP in scenarios BB_KDTD and BB_KDST are due to the light-limited leaves, that is, leaves in the lower canopy when radiation is abundant and leaves when radiation is limited. Therefore, the parameters that impact electron transport rate computation would result in a biased light-limited photosynthetic rate. However, most existing LSMs are not capable of accurately representing these trait-, temperature-, and environment-dependent parameters, as these LSMs use broadband canopy RT schemes. Thus, actions need to be taken to address this problem if these LSMs do not shift to a hyperspectral canopy RT scheme.

First, broadband reflectance and transmittance maps based on leaf traits such as chlorophyll content and leaf mass per area can be derived offline using models like PROSPECT and CliMA Land (Féret et al., 2021; Wang et al., 2023). These maps with spatial and temporal variations can supersede the look-up tables based on plant functional types used in most LSMs. This step addresses the issue in f_{APAR}, and will help not only photosynthesis but also the leaf energy balance modeling.

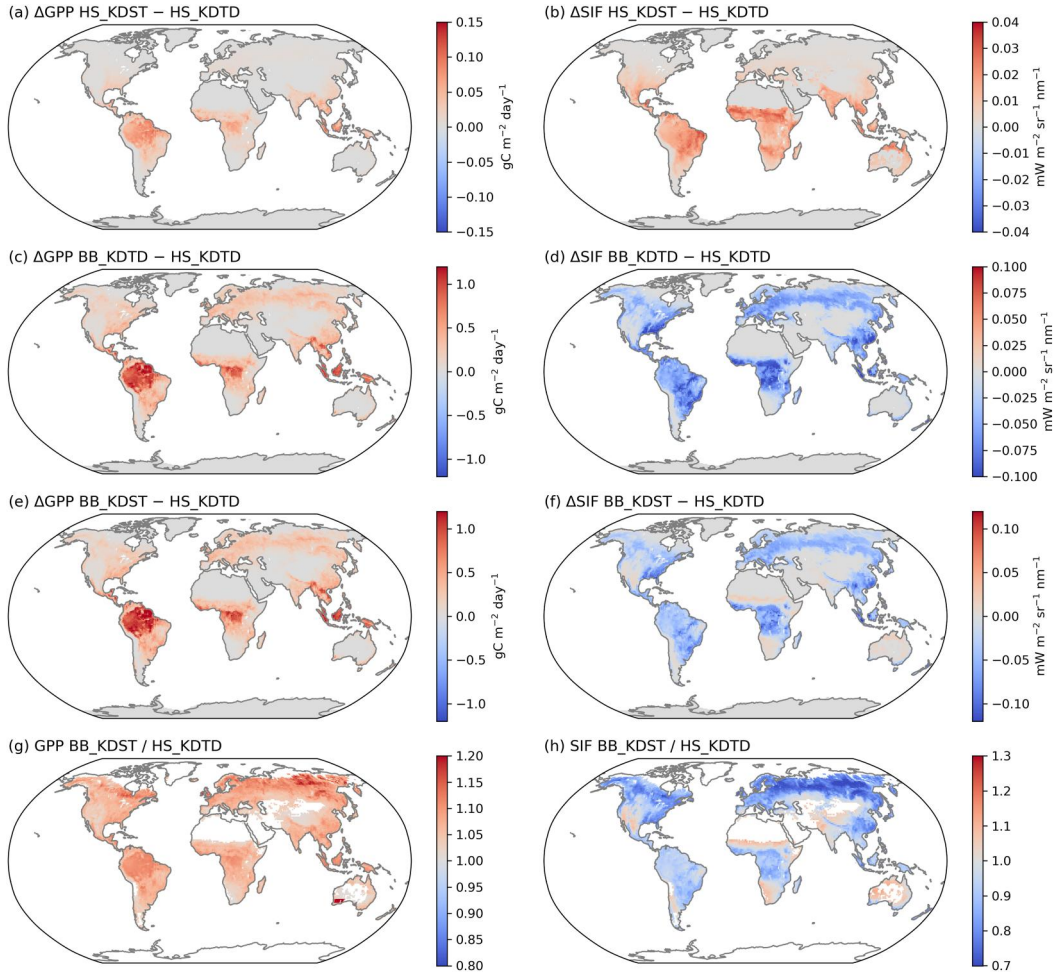

Figure 4. Difference in CliMA Land modeled GPP and SIF among scenarios. (a) HS_KDST − HS_KDTD GPP. (b) HS_KDST − HS_KDTD SIF at 740 nm. (c) BB_KDTD − HS_KDTD GPP. (d) BB_KDTD − HS_KDTD SIF. (e) BB_KDST − HS_KDTD GPP. (f) BB_KDST − HS_KDTD SIF. (g) BB_KDST/HS_KDTD GPP. (h) BB_KDST/HS_KDTD SIF. HS for hyperspectral RT mode, BB for broadband RT mode, KDTD for temperature-dependent K_D, and KDST for constant K_D.

Table 2
R^2 of the General Linear Models of ΔGPP and ΔSIF

Linear model	ΔGPP	ΔSIF
$Y \sim$ LMA	0.00	0.01
$Y \sim$ Chl	0.15	0.05
$Y \sim$ CI	0.42	0.23
$Y \sim$ LAI	0.87	0.30
$Y \sim$ LAI + LMA	0.87	0.29
$Y \sim$ LAI + CI	0.87	0.31
$Y \sim$ LAI + Chl	0.88	0.61
$Y \sim$ LAI + Chl + CI	0.88	0.62
$Y \sim$ LAI + Chl + LMA	0.87	0.64
$Y \sim$ LAI + Chl + CI + LMA	0.88	0.64

Second, an empirical parameterization of f_{PPAR} based on leaf traits and leaf position in a canopy (z from 0 for top to 1 for bottom) could help reduce the bias in modeled electron transport rate, for example, $f_{PPAR} = f(\text{Chl}, z)$. For example, we randomly combine LAI from 0.5 to 6, Chl from 10 to 80, and compute f_{PPAR} at different depths of a canopy using CliMA Land. We find that the computed f_{PPAR} for sunlit and shaded leaves at different canopy depths can be fitted using an empirical function (Figure 6):

$$f_{PPAR} = k_z \cdot z + k_{LAI} \cdot \text{LAI} + k_{Chl} \cdot \log[\log(\text{Chl})] + l. \quad (7)$$

The fitting parameters are $k_z = -0.0199$, $k_{LAI} = 0.00124$, $k_{Chl} = 0.210$, and $l = 0.511$ for the sunlit leaves; and $k_z = -0.0550$, $k_{LAI} = -0.00310$, $k_{Chl} = 0.176$, and $l = 0.549$ for the shaded leaves. The fitting parameters are $k_z = -0.0375$, $k_{LAI} = -0.000930$, $k_{Chl} = 0.193$, and $l = 0.530$ for the sunlit and shaded leaves combined.

Third, the temperature-dependent K_D can be readily modeled in existing LSMs using leaf temperature, and $\Phi_{PSII,max}$ needs to be changed accordingly.

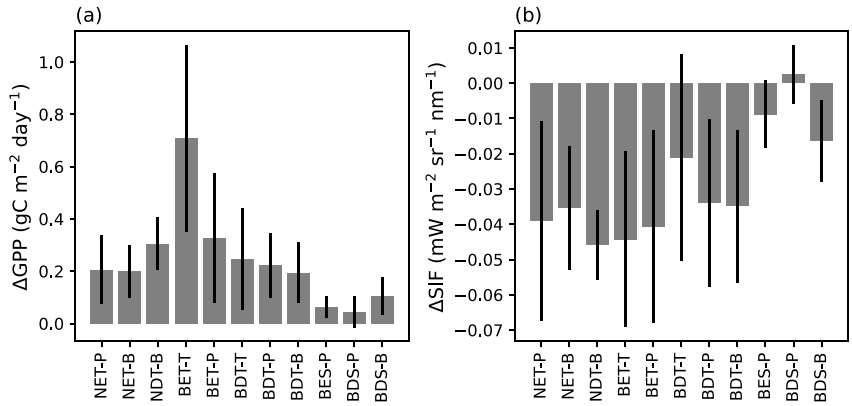

Figure 5. Difference in CliMA Land modeled GPP and SIF between BB_KDST and HS_KDTD scenarios. (a) ΔGPP for different PFTs. (b) ΔSIF for different PFTs.

While these improvements would require the traditional LSMs to rewire the hard-coded canopy RT and photosynthesis modules, they could substantially reduce the model biases in simulated energy balance, electron transport, and canopy assimilation.

We examined whether the above suggestions help reduce the inconsistency between hyperspectral and broadband RT models and minimize the difference in modeled GPP. We ran CliMA Land to simulate the GPP and SIF in a diurnal cycle using three RT models: (a) hyperspectral RT model, (b) PAR + NIR broadband RT model using leaf reflectance and transmittance from CLM look-up table (with K_D temperature dependence), and (c) PAR + NIR broadband model with corrections made. The corrections were that leaf broadband reflectance and transmittance for PAR and NIR were computed from leaf traits used in the hyperspectral RT model and that f_{PPAR} was computed using Equation 7 with the parameter sets fitted for sunlit and shaded leaves combined. We ran the model for two example sites, and our simulations showed that the GPP of the correction-made broadband RT model better agreed with the hyperspectral RT model values (Figure 7). However, the modeled SIF using the correction-made broadband RT model did not always show improvements (Figure 7). Thus, if accurate SIF modeling is desired, we recommend using hyperspectral RT models rather than a fusion of hyperspectral and broadband RT models. Notably, the suggested corrections hold great potential in improving the broadband RT model that is used in most LSMs.

We note here that the results in Figure 6 are based on the Reference Air Mass 1.5 Spectra from the American Society for Testing and Materials (ASTM) G-173. Thus, using the coefficients along with any light source different from the ATM G0173 Reference Air Mass 1.5 Spectra would result in different results (e.g., when the diffuse light faction is different). Consequently, the ultimate solution for this light-, plant trait-, and temperature-dependent molding of canopy RT, leaf electron transport, and photosynthesis would require the implementation

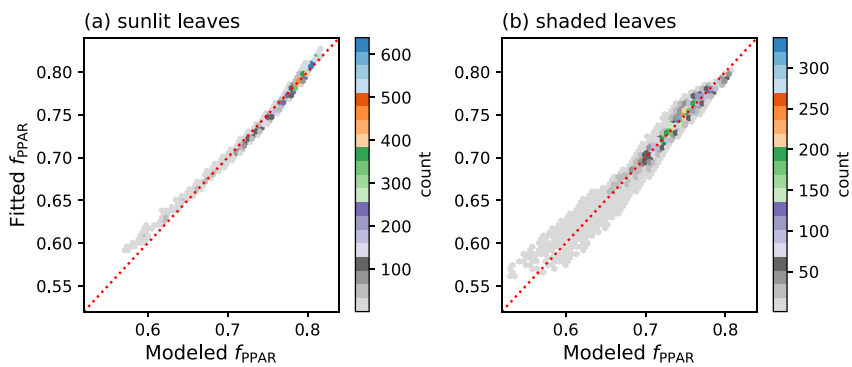

Figure 6. Empirical fitting of CliMA Land modeled f_{PPAR}. The f_{PPAR} is computed for leaves at different depths of a canopy with random LAI and Chl (LAI from 0.5 to 6; Chl from 5 to 80 μg cm^{-2}). (a) Comparison of the sunlit leaves. The black dots plot the point comparisons, and the red line plots the 1:1 line. (b) Comparison of the shaded leaves.

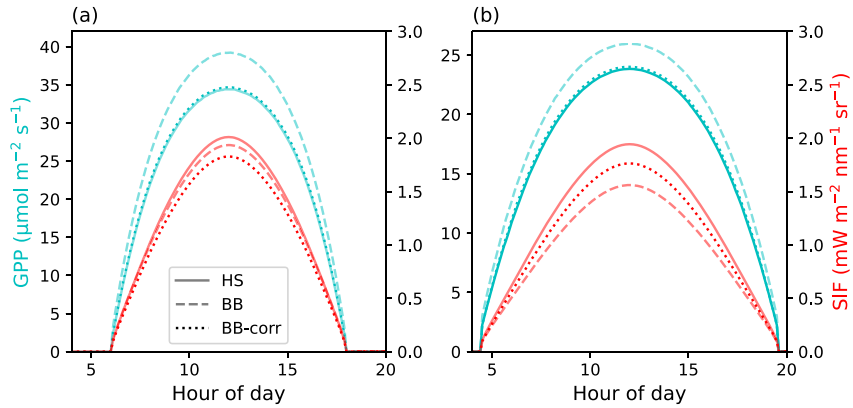

Figure 7. Comparison between modeled GPP and SIF in a diurnal cycle. Solid curves plot the GPP and SIF modeled using the hyperspectral RT module, dashed curves plot those using the broadband RT model, and dotted curves plot those using the broadband model with corrections. (a) Plant with LAI = 4 and Chl = 60 μg cm^{-2} at the equator, the reflectance for PAR and NIR are 0.10 and 0.45, and the transmittance for PAR and NIR are 0.05 and 0.25, respectively. (b) Plant with LAI = 4 and Chl = 60 μg cm^{-2} at 45°N, the reflectance for PAR and NIR are 0.07 and 0.35, and the transmittance for PAR and NIR are 0.05 and 0.10, respectively.

of a hyperspectral atmosphere RT module to account for the spatial and temporal variations of the direct and diffuse light spectra (Jeyaram et al., 2022; Sanghavi et al., 2014).

5. Conclusion

Electron transport in photosynthesis machinery is impacted by plant traits (such as chlorophyll content and leaf mass per area) and the environment (such as light source). However, this level of complexity has been overlooked by the traditional LSMs that model broadband canopy RT. Using a next-generation LSM that models hyperspectral canopy RT—CliMA Land, we explored how the implementation of plant trait-, temperature-, and environment-dependent electron transport may impact the global modeling of canopy RT and electron transport, and thus photosynthesis and fluorescence. We found that the electron transport parameterization used in the traditional LSMs would overestimate photosynthesis globally but underestimate fluorescence in most areas. We discussed the potential correction approaches that can be undertaken by the traditional LSMs, including (a) superseding the look-up tables of leaf reflectance and transmittance with spatially and temporally variant maps of leaf-level reflectance and transmittance, and (b) employing an empirical function to compute f_{PPAR} based on LAI, Chl, and leaf location in a canopy. We believe that the use of a more realistic representation of canopy RT and leaf electron transport would help improve the model predictive skills of the LSMs.

Conflict of Interest

The authors declare no conflicts of interest relevant to this study.

Data Availability Statement

We coded our model and did the analysis using Julia (version 1.10.0). The leaf level and global scale simulations were done using CliMA Land, which is available from the project website: https://github.com/CliMA/Land under the Apache 2.0 License. The exact version of the model used to produce the results used in this paper is archived on Zenodo (Wang & Frankenberg, 2024a). The global CliMA Land simulation with a tag of "a11_gm3_wd1" can be found at Wang and Frankenberg (2024b).

Acknowledgments
This research has been supported by the National Aeronautics and Space Administration (NASA) Carbon Cycle Science Grant 80NSSC21K1712 and OCO 2/3 Science Team Grant 80NSSC21K1075 awarded to Christian Frankenberg.

References

Allen, J. F., Bennett, J., Steinback, K. E., & Arntzen, C. J. (1981). Chloroplast protein phosphorylation couples plastoquinone redox state to distribution of excitation energy between photosystems. *Nature*, *291*(5810), 25–29. https://doi.org/10.1038/291025a0

Anderegg, W. R. L., Klein, T., Bartlett, M., Sack, L., Pellegrini, A. F. A., Choat, B., & Jansen, S. (2016). Meta-analysis reveals that hydraulic traits explain cross-species patterns of drought-induced tree mortality across the globe. *Proceedings of the National Academy of Sciences*, *113*(18), 5024–5029. https://doi.org/10.1073/pnas.1525678113

Ball, J. T., Woodrow, I. E., & Berry, J. A. (1987). A model predicting stomatal conductance and its contribution to the control of photosynthesis under different environmental conditions. In J. Biggins (Ed.), *Progress in photosynthesis research* (pp. 221–224). Springer.

Braghiere, R. K., Wang, Y., Doughty, R., Sousa, D., Magney, T., Widlowski, J.-L., et al. (2021). Accounting for canopy structure improves hyperspectral radiative transfer and sun-induced chlorophyll fluorescence representations in a new generation Earth System model. *Remote Sensing of Environment*, *261*, 112497. https://doi.org/10.1016/j.rse.2021.112497

Braghiere, R. K., Wang, Y., Gagne-Landmann, A., Brodrick, P. G., Bloom, A. A., Norton, A. J., et al. (2023). The importance of hyperspectral soil albedo information for improving Earth system model projections. *AGU Advances*, *4*, e2023AV000910. https://doi.org/10.1029/2020AV000910

Butler, E. E., Datta, A., Flores-Moreno, H., Chen, M., Wythers, K. R., Fazayeli, F., et al. (2017). Mapping local and global variability in plant trait distributions. *Proceedings of the National Academy of Sciences*, *114*(51), E10937–E10946. https://doi.org/10.1073/pnas.1708984114

Campbell, G. S., & Norman, J. M. (1998). *An introduction to environmental biophysics*. Springer Science & Business Media.

Collatz, G. J., Ribas-Carbo, M., & Berry, J. (1992). Coupled photosynthesis-stomatal conductance model for leaves of C_4 plants. *Functional Plant Biology*, *19*(5), 519–538. https://doi.org/10.1071/pp9920519

Croft, H., Chen, J., Wang, R., Mo, G., Luo, S., Luo, X., et al. (2020). The global distribution of leaf chlorophyll content. *Remote Sensing of Environment*, *236*, 111479. https://doi.org/10.1016/j.rse.2019.111479

Dai, Y., Xin, Q., Wei, N., Zhang, Y., Shangguan, W., Yuan, H., et al. (2019). A global high-resolution data set of soil hydraulic and thermal properties for land surface modeling. *Journal of Advances in Modeling Earth Systems*, *11*(9), 2996–3023. https://doi.org/10.1029/2019ms001784

Evans, J. R. (1996). Developmental constraints on photosynthesis: Effects of light and nutrition. In *Photosynthesis and the environment* (pp. 281–304). Springer.

Farquhar, G. D., von Caemmerer, S., & Berry, J. A. (1980). A biochemical model of photosynthetic CO_2 assimilation in leaves of C_3 species. *Planta*, *149*(1), 78–90. https://doi.org/10.1007/bf00386231

Féret, J.-B., Berger, K., De Boissieu, F., & Malenovskỳ, Z. (2021). PROSPECT-PRO for estimating content of nitrogen-containing leaf proteins and other carbon-based constituents. *Remote Sensing of Environment*, *252*, 112173. https://doi.org/10.1016/j.rse.2020.112173

Féret, J.-B., Gitelson, A., Noble, S., & Jacquemoud, S. (2017). PROSPECT-D: Towards modeling leaf optical properties through a complete lifecycle. *Remote Sensing of Environment*, *193*, 204–215. https://doi.org/10.1016/j.rse.2017.03.004

Friedlingstein, P., O'Sullivan, M., Jones, M. W., Andrew, R. M., Gregor, L., Hauck, J., et al. (2022). Global carbon budget 2022. *Earth System Science Data*, *14*(11), 4811–4900. https://doi.org/10.5194/essd-14-4811-2022

Grassi, G., Meir, P., Cromer, R., Tompkins, D., & Jarvis, P. (2002). Photosynthetic parameters in seedlings of *Eucalyptus grandis* as affected by rate of nitrogen supply. *Plant, Cell and Environment*, *25*(12), 1677–1688. https://doi.org/10.1046/j.1365-3040.2002.00946.x

Harley, P. C., Loreto, F., Di Marco, G., & Sharkey, T. D. (1992). Theoretical considerations when estimating the mesophyll conductance to CO_2 flux by analysis of the response of photosynthesis to CO_2. *Plant Physiology*, *98*(4), 1429–1436. https://doi.org/10.1104/pp.98.4.1429

Hersbach, H., Bell, B., Berrisford, P., Hirahara, S., Horányi, A., Muñoz-Sabater, J., et al. (2020). The ERA5 global reanalysis. *Quarterly Journal of the Royal Meteorological Society*, *146*(730), 1999–2049. https://doi.org/10.1002/qj.3803

Hogewoning, S. W., Wientjes, E., Douwstra, P., Trouwborst, G., Van Ieperen, W., Croce, R., & Harbinson, J. (2012). Photosynthetic quantum yield dynamics: From photosystems to leaves. *The Plant Cell*, *24*(5), 1921–1935. https://doi.org/10.1105/tpc.112.097972

Jacquemoud, S., & Baret, F. (1990). PROSPECT: A model of leaf optical properties spectra. *Remote Sensing of Environment*, *34*(2), 75–91. https://doi.org/10.1016/0034-4257(90)90100-z

Jeyaram, R., Sanghavi, S., & Frankenberg, C. (2022). vSmartMOM.jl: An open-source Julia package for atmospheric radiative transfer and remote sensing tools. *Journal of Open Source Software*, *7*(80), 4575. https://doi.org/10.21105/joss.04575

Jiang, C., & Fang, H. (2019). GSV: A general model for hyperspectral soil reflectance simulation. *International Journal of Applied Earth Observation and Geoinformation*, *83*, 101932. https://doi.org/10.1016/j.jag.2019.101932

Johnson, J., & Berry, J. (2021). The role of Cytochrome b_6f in the control of steady-state photosynthesis: A conceptual and quantitative model. *Photosynthesis Research*, *148*(3), 101–136. https://doi.org/10.1007/s11120-021-00840-4

Laisk, A., Oja, V., Eichelmann, H., & Dall'Osto, L. (2014). Action spectra of photosystems II and I and quantum yield of photosynthesis in leaves in state. *Biochimica et Biophysica Acta (BBA)-Bioenergetics*, *1837*(2), 315–325. https://doi.org/10.1016/j.bbabio.2013.12.001

Lawrence, D. M., Fisher, R. A., Koven, C. D., Oleson, K. W., Swenson, S. C., Bonan, G., et al. (2019). The community land model version 5: Description of new features, benchmarking, and impact of forcing uncertainty. *Journal of Advances in Modeling Earth Systems*, *11*(12), 4245–4287. https://doi.org/10.1029/2018ms001583

Lawrence, P. J., & Chase, T. N. (2007). Representing a new MODIS consistent land surface in the Community Land Model (CLM 3.0). *Journal of Geophysical Research*, *112*(G1), G01023. https://doi.org/10.1029/2006JG000168

Leuning, R. (1995). A critical appraisal of a combined stomatal-photosynthesis model for C_3 plants. *Plant, Cell and Environment*, *18*(4), 339–355. https://doi.org/10.1111/j.1365-3040.1995.tb00370.x

Li, F., Hao, D., Zhu, Q., Yuan, K., Braghiere, R. K., He, L., et al. (2023). Vegetation clumping modulates global photosynthesis through adjusting canopy light environment. *Global Change Biology*, *29*(3), 731–746. https://doi.org/10.1111/gcb.16503

Luo, X., Keenan, T. F., Chen, J. M., Croft, H., Colin Prentice, I., Smith, N. G., et al. (2021). Global variation in the fraction of leaf nitrogen allocated to photosynthesis. *Nature Communications*, *12*(1), 4866. https://doi.org/10.1038/s41467-021-25163-9

Magney, T. S., Bowling, D. R., Logan, B. A., Grossmann, K., Stutz, J., Blanken, P. D., et al. (2019). Mechanistic evidence for tracking the seasonality of photosynthesis with solar-induced fluorescence. *Proceedings of the National Academy of Sciences*, *116*(24), 11640–11645. https://doi.org/10.1073/pnas.1900278116

McDowell, N. G., & Allen, C. D. (2015). Darcy's law predicts widespread forest mortality under climate warming. *Nature Climate Change*, *5*(7), 669–672. https://doi.org/10.1038/nclimate2641

McDowell, N. G., Pockman, W. T., Allen, C. D., Breshears, D. D., Cobb, N., Kolb, T., et al. (2008). Mechanisms of plant survival and mortality during drought: Why do some plants survive while others succumb to drought? *New Phytologist*, *178*(4), 719–739. https://doi.org/10.1111/j.1469-8137.2008.02436.x

Medlyn, B. E., Dreyer, E., Ellsworth, D., Forstreuter, M., Harley, P. C., Kirschbaum, M. U. F., et al. (2002). Temperature response of parameters of a biochemically based model of photosynthesis. II. A review of experimental data. Plant. *Cell & Environment*, *25*(9), 1167–1179. https://doi.org/10.1046/j.1365-3040.2002.00891.x

Medlyn, B. E., Duursma, R. A., Eamus, D., Ellsworth, D. S., Prentice, I. C., Barton, C. V. M., et al. (2011). Reconciling the optimal and empirical approaches to modelling stomatal conductance. *Global Change Biology*, *17*(6), 2134–2144. https://doi.org/10.1111/j.1365-2486.2010.02375.x

Norman, J. M. (1982). Simulation of microclimates. *Biometeorology in Integrated Pest Management*, 65–99. https://doi.org/10.1016/b978-0-12-332850-2.50009-8

Porcar-Castell, A. (2011). A high-resolution portrait of the annual dynamics of photochemical and non-photochemical quenching in needles of *Pinus sylvestris*. *Physiologia Plantarum*, *143*(2), 139–153. https://doi.org/10.1111/j.1399-3054.2011.01488.x

Porcar-Castell, A., Malenovský, Z., Magney, T., Van Wittenberghe, S., Fernández-Marín, B., Maignan, F., et al. (2021). Chlorophyll a fluorescence illuminates a path connecting plant molecular biology to earth-system science. *Nature Plants*, *7*(8), 998–1009. https://doi.org/10.1038/s41477-021-00980-4

Quebbeman, J. A., & Ramirez, J. A. (2016). Optimal allocation of leaf-level nitrogen: Implications for covariation of V_{cmax} and J_{max} and photosynthetic downregulation. *Journal of Geophysical Research: Biogeosciences*, *121*(9), 2464–2475. https://doi.org/10.1002/2016jg003473

Raczka, B., Porcar-Castell, A., Magney, T., Lee, J. E., Köhler, P., Frankenberg, C., et al. (2019). Sustained nonphotochemical quenching shapes the seasonal pattern of solar-induced fluorescence at a high-elevation evergreen forest. *Journal of Geophysical Research: Biogeosciences*, *124*(7), 2005–2020. https://doi.org/10.1029/2018jg004883

Sabot, M. E., De Kauwe, M. G., Pitman, A. J., Medlyn, B. E., Ellsworth, D. S., Martin-StPaul, N., et al. (2022). One stomatal model to rule them all? Towards improved representation of carbon and water exchange in global models. *Journal of Advances in Modeling Earth Systems*, *14*(4), e2021MS002761. https://doi.org/10.1029/2021MS002761

Sanghavi, S., Davis, A. B., & Eldering, A. (2014). vSmartMOM: A vector matrix operator method-based radiative transfer model linearized with respect to aerosol properties. *Journal of Quantitative Spectroscopy and Radiative Transfer*, *133*, 412–433. https://doi.org/10.1016/j.jqsrt.2013.09.004

Schlesinger, W. H., & Jasechko, S. (2014). Transpiration in the global water cycle. *Agricultural and Forest Meteorology*, *189*, 115–117. https://doi.org/10.1016/j.agrformet.2014.01.011

Simard, M., Pinto, N., Fisher, J. B., & Baccini, A. (2011). Mapping forest canopy height globally with spaceborne lidar. *Journal of Geophysical Research*, *116*(G4), G4021. https://doi.org/10.1029/2011JG001708

Sperry, J. S., Venturas, M. D., Anderegg, W. R. L., Mencuccini, M., Mackay, D. S., Wang, Y., & Love, D. M. (2017). Predicting stomatal responses to the environment from the optimization of photosynthetic gain and hydraulic cost. *Plant, Cell and Environment*, *40*(6), 816–830. https://doi.org/10.1111/pce.12852

Sperry, J. S., Venturas, M. D., Todd, H. N., Trugman, A. T., Anderegg, W. R. L., Wang, Y., & Tai, X. (2019). The impact of rising CO_2 and acclimation on the response of US forests to global warming. *Proceedings of the National Academy of Sciences*, *116*(51), 25734–25744. https://doi.org/10.1073/pnas.1913072116

Tyree, M. T., & Zimmermann, M. H. (2002). *Xylem structure and the ascent of sap* (2nd ed.). Springer. https://doi.org/10.1007/978-3-662-04931-0

van der Tol, C., Berry, J., Campbell, P., & Rascher, U. (2014). Models of fluorescence and photosynthesis for interpreting measurements of solar-induced chlorophyll fluorescence. *Journal of Geophysical Research: Biogeosciences*, *119*(12), 2312–2327. https://doi.org/10.1002/2014jg002713

van der Tol, C., Verhoef, W., Timmermans, J., Verhoef, A., & Su, Z. (2009). An integrated model of soil-canopy spectral radiances, photosynthesis, fluorescence, temperature and energy balance. *Biogeosciences*, *6*(12), 3109–3129. https://doi.org/10.5194/bg-6-3109-2009

Venturas, M. D., Sperry, J. S., & Hacke, U. G. (2017). Plant xylem hydraulics: What we understand, current research, and future challenges. *Journal of Integrative Plant Biology*, *59*(6), 356–389. https://doi.org/10.1111/jipb.12534

Walker, A. P., Beckerman, A. P., Gu, L., Kattge, J., Cernusak, L. A., Domingues, T. F., et al. (2014). The relationship of leaf photosynthetic traits–V_{cmax} and J_{max}–to leaf nitrogen, leaf phosphorus, and specific leaf area: A meta-analysis and modeling study. *Ecology and Evolution*, *4*(16), 3218–3235. https://doi.org/10.1002/ece3.1173

Wang, Y., Anderegg, W. R., Venturas, M. D., Trugman, A. T., Yu, K., & Frankenberg, C. (2021). Optimization theory explains nighttime stomatal responses. *New Phytologist*, *230*(4), 1550–1561. https://doi.org/10.1111/nph.17267

Wang, Y., Braghiere, R., Longo, M., Norton, A., Köhler, P., Doughty, R., et al. (2023). Modeling global vegetation gross primary productivity, transpiration and hyperspectral canopy radiative transfer simultaneously using a next generation land surface model—CliMA Land. *Journal of Advances in Modeling Earth Systems*, *15*(3), e2021MS002964. https://doi.org/10.1029/2021MS002964

Wang, Y., & Frankenberg, C. (2022). On the impact of canopy model complexity on simulated carbon, water, and solar-induced chlorophyll fluorescence fluxes. *Biogeosciences*, *19*(1), 29–45. https://doi.org/10.5194/bg-19-29-2022

Wang, Y., & Frankenberg, C. (2024a). CliMA Land code archive (version a11) [Software]. *Zenodo*. https://doi.org/10.5281/zenodo.10652942

Wang, Y., & Frankenberg, C. (2024b). CliMA Land global simulations archive (version a11) [Dataset]. *Zenodo*. https://doi.org/10.5281/zenodo.10652972

Wang, Y., Köhler, P., Braghiere, R. K., Longo, M., Doughty, R., Bloom, A. A., & Frankenberg, C. (2022). GriddingMachine, a database and software for Earth system modeling at global and regional scales. *Scientific Data*, *9*(1), 258. https://doi.org/10.1038/s41597-022-01346-x

Wang, Y., Köhler, P., He, L., Doughty, R., Braghiere, R. K., Wood, J. D., & Frankenberg, C. (2021). Testing stomatal models at the stand level in deciduous angiosperm and evergreen gymnosperm forests using clima land (v0.1). *Geoscientific Model Development*, *14*(11), 6741–6763. https://doi.org/10.5194/gmd-14-6741-2021

Wang, Y., Sperry, J. S., Anderegg, W. R. L., Venturas, M. D., & Trugman, A. T. (2020). A theoretical and empirical assessment of stomatal optimization modeling. *New Phytologist*, *227*(2), 311–325. https://doi.org/10.1111/nph.16572

Wei, S., Fang, H., Schaaf, C. B., He, L., & Chen, J. M. (2019). Global 500 m clumping index product derived from MODIS BRDF data (2001–2017). *Remote Sensing of Environment*, *232*, 111296. https://doi.org/10.1016/j.rse.2019.111296

Wolf, A., Anderegg, W. R. L., & Pacala, S. W. (2016). Optimal stomatal behavior with competition for water and risk of hydraulic impairment. *Proceedings of the National Academy of Sciences*, *113*(46), E7222–E7230. https://doi.org/10.1073/pnas.1615144113

Yamazaki, D., Ikeshima, D., Tawatari, R., Yamaguchi, T., O'Loughlin, F., Neal, J. C., et al. (2017). A high-accuracy map of global terrain elevations. *Geophysical Research Letters*, *44*(11), 5844–5853. https://doi.org/10.1002/2017gl072874

Yang, P., Verhoef, W., & van der Tol, C. (2017). The mSCOPE model: A simple adaptation to the SCOPE model to describe reflectance, fluorescence and photosynthesis of vertically heterogeneous canopies. *Remote Sensing of Environment*, *201*, 1–11. https://doi.org/10.1016/j.rse.2017.08.029

Yuan, H., Dai, Y., Xiao, Z., Ji, D., & Shangguan, W. (2011). Reprocessing the MODIS Leaf Area Index products for land surface and climate modelling. *Remote Sensing of Environment*, *115*(5), 1171–1187. https://doi.org/10.1016/j.rse.2011.01.001

Zhen, S., & Bugbee, B. (2020). Far-red photons have equivalent efficiency to traditional photosynthetic photons: Implications for redefining photosynthetically active radiation. *Plant, Cell and Environment*, *43*(5), 1259–1272. https://doi.org/10.1111/pce.13730